Model of Two-Phase Flow and Flooding Dynamics in Polymer Electrolyte Fuel Cells

Hua Meng* and Chao-Yang Wang*,z

Electrochemical Engine Center and Department of Mechanical and Nuclear Engineering, The Pennsylvania State University, University Park, Pennsylvania 16802, USA

A mathematical model for two-phase flow and flooding dynamics in polymer electrolyte fuel cells (PEFCs) has been developed based on recent experimental observations. This three-dimensional PEFC model consists of four submodels to account for two-phase phenomena, including a catalyst coverage model in the catalyst layer, a two-phase transport model in the gas diffusion layer (GDL), a liquid coverage model at the GDL-channel interface, and a two-phase flow model in the gas channel (GC). The multiphase mixture (M^2) model is employed to describe liquid water transport in the GDL while a mist flow model is used in the gas channel. An interfacial coverage model by liquid water at the GDL/GC interface is developed, for the first time, to account for water droplet emergence on the GDL surface. The inclusion of this interfacial model not only gives the present two-phase model a capability to predict the cathode flooding effect on cell performance, but also ultimately removes the inability of prior two-phase models to correctly capture effects of the gas velocity (or stoichiometry) on cell performance.
© 2005 The Electrochemical Society. [DOI: 10.1149/1.1955007] All rights reserved.

Water management is a central issue in design and optimization of polymer electrolyte fuel cells (PEFCs). There are two well-understood reasons: first, the proton conductivity of the electrolyte membrane depends strongly on hydration; second, the presence of excessive liquid water covers catalyst sites in the catalyst layer as well as blocks the oxygen transport in the gas diffusion layer (GDL), resulting in substantial concentration polarization. Therefore, a delicate balance of water in the cell must be maintained to ensure proper operation. Because the oxygen reduction reaction (ORR) in the cathode catalyst layer produces water, prevention of liquid water flooding is especially crucial on the cathode side of the cell.

In the past decade, numerical modeling of PEFCs has received much attention. Many two- and three-dimensional models have been developed in which the computational fluid dynamics (CFD) method has been rigorously coupled with electrochemical phenomena.[1-5] Electron transport and heat-transfer phenomena have also been incorporated.[6-10] A parallel computing methodology has recently been introduced for large-scale PEFC simulations.[11] Although these single-phase or pseudo single-phase numerical models have already provided significant capabilities to study a multitude of physical phenomena in PEFCs, they are unable to capture the physics of liquid water formation and transport as well as the ensuing flooding effects.

Much effort has also been expended on the development of rigorous physical models for two-phase flow and flooding prediction. Wang et al.[12] first studied two-phase flow and liquid water transport on the cathode side of a PEFC based on the multiphase mixture model (M^2 model) originally developed by Wang and Cheng[13] and summarized by Wang and Cheng.[14] Although liquid water transport and two-phase formation were handled successfully, the predicted liquid water saturation could only reach a maximum value of 6.3%, resulting in negligible flooding effects. The same problem has also been encountered in studies of You and Liu,[15] Mazumder and Cole,[16] Pasaogullari and Wang,[17] and Berning and Djilali,[18] although different two-phase models have been adopted. The first three studies were based on the M^2 model, while the last one used the traditional two-fluid model.[19] While the M^2 and two-fluid models are expressed in different forms, they are mathematically equivalent. The two-phase flow and flooding effects have also been investigated by He et al.[20] for a PEFC with the interdigitated flow-field. In this study, a constant gradient of capillary force, instead of varying with the liquid saturation, was assumed. The predicted liquid saturation was also below 5%. In order to increase the value of liquid saturation and dramatize GDL flooding effects, Natarajan and

Nguyen[21] used an unrealistically small GDL permeability of 7.3 $\times 10^{-15}$ m^2 to fit their experimentally measured polarization curve. In addition, it is unclear whether the GDL was hydrophobic or hydrophilic in the two studies of Nguyen and co-workers.

Another more serious weakness in the prior two-phase models is that they cannot distinguish the vastly different behaviors of a hydrophobic vs. hydrophilic GDL. The numerical investigation of Pasaogullari and Wang[17] was carried out with a hydrophobic GDL while all the other studies were apparently for hydrophilic GDLs.[12,15,16,18]

Limited experimental data began to emerge in the literature on liquid water behaviors at the GDL surface and in the gas channel (GC).[22,23] The visualization data in these experimental works clearly showed that liquid water emerges from the GDL in the form of small droplets covering the GDL/GC interface. This interfacial behavior of liquid water could alter the transport characteristics inside the porous GDL. These data have, therefore, provided new evidence of flooding in the GDL and catalyst layer that should be included in a two-phase model. The readers should consult Wang[24] for a comprehensive review of fuel cell models and associated experimental diagnostics efforts.

To address the above-discussed unresolved issues, the present work aims to develop a novel model for two-phase flow and flooding dynamics in PEFCs, in which an interfacial liquid coverage submodel at the GDL surface is added as an essential component. Such a model will be capable of yielding a reasonably high liquid level inside the catalyst layer as the liquid saturation profile will start from nonzero at the GDL surface rather than zero as in all previous two-phase modeling studies. Furthermore, because the extent of liquid coverage at the GDL surface strongly depends on its wettability, the new model is able to differentiate the fundamental differences between hydrophilic and hydrophobic GDLs. Finally, it has been correlated experimentally that the droplet size before detachment, and hence the liquid coverage on the GDL surface, drastically increases with decreasing air velocity in the gas channel[25]; as such, the present model is expected to capture the dramatic effectiveness of increasing air stoichiometry to alleviate PEFC flooding, beyond the beneficial level of the increased oxidant concentration in the flow.

In the following, a comprehensive two-phase model is presented that tightly couples three-dimensional transport phenomena with interfacial and electrochemical processes. The model is subsequently used to explore the impact of the GDL interfacial liquid coverage on two-phase and flooding dynamics in a straight-channel PEFC.

Mathematical Model

In this section, a three-dimensional, two-phase, multicomponent model of PEFCs is presented. The energy equation is ignored in the

present study so as to focus on the impact of liquid coverage model at the GDL/GC interface on two-phase flow and flooding dynamics.

Conservation equations.— The conservation equations of mass, momentum, species, and proton and electron transport are numerically solved to obtain flow-field, species concentrations, phase potentials, and liquid water saturation throughout a fuel cell

Mass

$$\nabla(\rho \mathbf{u}) = 0 \qquad [1]$$

Momentum

$$\frac{1}{\varepsilon^2} \nabla (\rho \mathbf{u}\mathbf{u}) = - \nabla p + \nabla \tau + S_u \qquad [2]$$

Species

$$\nabla(\gamma_i \mathbf{u} C_i) = \nabla \left(\sum_k D_{i,k}^{eff} \nabla C_{i,k} \right) - \nabla \left(\sum_k \frac{C_{i,k}}{\rho_k} \mathbf{j}_k \right) + S_i \qquad [3]$$

Proton transport

$$\nabla(\kappa^{eff} \nabla \phi_e) + S_e = 0 \qquad [4]$$

Electron transport

$$\nabla(\sigma^{eff} \nabla \phi_s) + S_s = 0 \qquad [5]$$

The above conservation equations of mass, momentum, and species are derived based on the M^2 model[13] for two-phase flow and transport in porous media. In gas channels, the mist flow model has been applied to describe liquid water transport, in which water is assumed to exist in tiny droplets and travel with the gas velocity. Therefore, the conservation equations in the gas channel are simplified to a homogeneous single-phase form, as in the previous work.[9,11] A detailed description of the proton and electron transport equations can be found in Meng and Wang.[9]

Supplemental relations and mixture properties in the M^2 *model.*—In the conservation equations, Eq. 1-3, the mixture properties are all dependent on the liquid saturation, defined as the ratio of the liquid volume to the pore volume

$$s = \frac{V_l}{V_p} \qquad [6]$$

The mixture properties are defined as[13]
Molar concentration

$$C_i = C_{i,l}s + C_{i,g}(1 - s) \qquad [7]$$

Density

$$\rho = \rho_l s + \rho_g(1 - s) \qquad [8]$$

Relative permeabilities

$$k_{rl} = s^3 \qquad [9a]$$

$$k_{rg} = (1 - s)^3 \qquad [9b]$$

Kinematic viscosity

$$\nu = \left(\frac{k_{rl}}{\nu_l} + \frac{k_{rg}}{\nu_g} \right)^{-1} \qquad [10]$$

Relative mobilities

$$\lambda_l = \frac{k_{rl}}{\nu_l} \nu \qquad [11a]$$

$$\lambda_g = 1 - \lambda_l \qquad [11b]$$

The advection correction factor in Eq. 3 can be derived as[13]

$$\gamma_i = \frac{\rho(\lambda_l C_{i,l}/\rho_l + \lambda_g C_{i,g}/\rho_g)}{C_i} \qquad [12]$$

The mass flux, $\mathbf{j}_k$, can be expressed as

$$\mathbf{j}_l = - \mathbf{j}_g = \frac{K\lambda_l\lambda_g}{\nu} \nabla p_c \qquad [13]$$

where the capillary pressure, p_c, is defined as

$$p_c = p_g - p_l \qquad [14]$$

The capillary pressure can be further expressed as

$$p_c = \left(\frac{\varepsilon}{K} \right)^{1/2} \sigma \cos \theta_c J(s) \qquad [15]$$

where $J(s)$ is the well-known Leverett's function, which takes the following form[26]

$$J(s) = \begin{cases} 1.417(1-s) - 2.120(1-s)^2 + 1.263(1-s)^3 & \theta_c \leq 90° \\ 1.417s - 2.120(1-s)^2 + 1.263(1-s)^3 & \theta_c > 90° \end{cases} \qquad [16]$$

In Eq. 16, the porous material is hydrophilic when $\theta_c \leq 90°$, while it is hydrophobic when $\theta_c > 90°$.

Inside the two-phase zone, thermodynamic equilibrium between the gas and liquid phases is assumed to prevail due to the large liquid-gas interfacial area present inside GDL pores. Thus, the water vapor concentration in the two-phase zone takes the saturation value that depends on cell temperature. That is

$$C_{g,w} = C_{g,w}^{sat} \qquad [17]$$

Therefore, the liquid saturation in the two-phase zone can be back-calculated from the total molar concentration of water via Eq. 7 where the water concentration in the liquid is simply equal to ρ_l/Mw_{H_2O}.

Further details regarding the M^2 model and mixture properties can be found in Wang and Cheng.[13]

Source terms and physicochemical relations.— In Eq. 2, the source term, S_u, is added in the porous GDL and catalyst layer based on Darcy's law, i.e.

$$S_u = - \frac{\mu}{K}\mathbf{u} \qquad [18]$$

The species conservation equation is used for solving hydrogen, oxygen, and water concentrations. The source terms can be expressed in the following general form

$$S_i = - \frac{s_i \mathbf{j}}{nF} - \nabla \left(\frac{n_d}{F}\mathbf{i}_e \right) \qquad [19]$$

In Eq. 19, the first term on the right side, resulting from electrochemical kinetics, applies to all three species and appears in the catalyst layer, while the second term, resulting from electro-osmosis, is only relevant to the water-transport equation and appears inside the membrane and two catalyst layers. In deriving Eq. 19, electrochemical reactions are written in the following general form

$$\sum_i s_i M_i = ne^- \qquad [20]$$

See Meng and Wang[11] for more details.

The source terms in the proton- and electron-transport equations, Eq. 4 and 5, result from electrochemical kinetics and appear only in the catalyst layers such that

$$S_e = j \qquad [21]$$

$$S_s = - j \qquad [22]$$

The transfer current densities in these equations can be expressed as[3,9]

$$\text{Anode} \quad j = a^{eff} j_{0,a}^{ref} \left(\frac{c_{H_2}}{c_{H_2,ref}} \right)^{1/2} \left(\frac{\alpha_a + \alpha_c}{RT}F\eta \right) \qquad [23]$$

Cathode $j = -a^{\text{eff}} j_{0,c}^{\text{ref}} \left(\dfrac{c_{O_2}}{c_{O_2,\text{ref}}} \right) \exp\left(-\dfrac{\alpha_c}{RT} F\eta \right)$ [24]

where the surface overpotentials are defined as
Anode side

$$\eta = \phi_s - \phi_e \qquad\qquad [25]$$

Cathode side

$$\eta = \phi_s - \phi_e - U_{\text{oc}} \qquad\qquad [26]$$

The open-circuit potential, U_{oc}, is given by[27]

$$U_{\text{oc}} = 1.23 - 0.9 \times 10^{-3}(T - 298) \qquad [27]$$

The electro-osmotic drag coefficient in Eq. 19, n_d, can be expressed as[28,29]

$$n_d = \begin{cases} 1.0 & \text{for } \lambda \leq 14 \\ 1.5/8(\lambda - 14) + 1.0 & \text{otherwise} \end{cases} \qquad [28]$$

Membrane water content, defined as the number of water molecules per sulfonic acid group (SO_3^-), is determined by the water activity at the interface of the membrane and gas phases in thermodynamic equilibrium[30]

$$\lambda = \begin{cases} 0.043 + 17.18a - 39.85a^2 + 36.0a^3 & 0 < a \leq 1 \\ 14 + 1.4(a - 1) & 1 < a \leq 3 \\ 16.8 & a > 3 \end{cases} \quad [29]$$

Water diffusion through the membrane is calculated based on the empirical water diffusivity of Motupally et al.[31]

$$D_w^m = \begin{cases} 3.1 \times 10^{-7}\lambda(e^{0.28\lambda} - 1)e^{[-2346/T]} & 0 < \lambda \leq 3 \\ 4.17 \times 10^{-8}\lambda(1 + 161e^{-\lambda})e^{[-2346/T]} & \text{otherwise} \end{cases}$$

[30]

The dependence of proton conductivity on water content is calculated using the following empirical expression of Springer et al.[30]

$$\kappa = (0.5139\lambda - 0.326)\exp\left[1268\left(\dfrac{1}{303} - \dfrac{1}{T} \right) \right] \qquad [31]$$

In the present model, the Bruggeman correction is used to account for effective transport properties in porous media. Further details regarding the source terms and the physicochemical relations can be found in Meng and Wang.[9,11]

Two-phase submodels in GDL and catalyst layer.— The presence of liquid water in the porous GDL hinders gas-phase species diffusion, especially the oxygen transport on the cathode side because of its lower diffusivity. This hindrance effect is described via the effective gas diffusivity in the GDL given by

$$D_i^{\text{eff}} = D_i \varepsilon^{1.5}(1 - s)^{\tau_d} \qquad [32]$$

A similar expression has also been proposed in Nam and Kaviany.[32]
Liquid water in the catalyst layer covers portions of catalyst sites, decreasing the electrochemically active surface area. This effect is modeled as

$$a^{\text{eff}} = (1 - s)^{\tau_c} a \qquad [33]$$

This submodel has been commonly employed in the literature, where the coefficient, τ_c, is generally set to unity.[12,20] This submodel is based on the fact that oxygen dissolution in liquid water is essentially zero and hence its diffusion through the liquid film to catalyst sites is negligible, and the assumption that the morphology of liquid water in the catalyst layer is such that the surface coverage is directly proportional to the liquid volume fraction.

Liquid coverage submodel at the GDL/GC interface.— As shown in recent experimental observations,[22,23,25] liquid water emerges from the porous GDL in the form of droplets. The droplet detachment diameter along with the droplet population density at the GDL surface determines the interfacial liquid

saturation, which is in turn a key parameter to influence the level of flooding inside the GDL and catalyst layer. Zhang et al.[25] most recently found that the interfacial liquid saturation correlates strongly with the channel gas velocity as the droplet detachment diameter from the GDL surface results from the balance between the drag force of air core flow on the drop and the drop's surface adhesion with the GDL. In addition, because liquid tends to form a droplet or a film at the hydrophobic and hydrophilic GDL surfaces, respectively, the interfacial liquid saturation at the GDL/GC interface is also a function of the GDL surface wettability, i.e., contact angle. Furthermore, the droplet population density at the GDL surface, i.e., the number of sites activated with droplet emergence, is related to the local current density. Therefore, the interfacial liquid saturation is also a function of the current density. To summarize, we have

$$s_{\text{int}} = S(\mathbf{u}, \theta_c, I) \qquad [34]$$

The exact form of this interfacial saturation function is determined by experimental measurements for a specific GDL material system.

In the present work focusing on exploring fundamental physics and numerical behaviors of two-phase dynamics with and without interfacial liquid coverage at the GDL surface, we consider a hydrophobic carbon paper GDL with a contact angle of 110°. Moreover, the following simplified function of the interfacial liquid saturation is assumed for the purpose of a parametric study

$$s_{\text{int}} = S(\mathbf{u}, \theta_c) f(I) \qquad [35]$$

where the current density function, $f(I)$, takes the following form

$$f(I) = \begin{cases} 0 & V_c > 0.8 \\ \dfrac{0.8 - V_c}{0.2} & 0.6 < V_c \leq 0.8 \\ 1 & V_c \leq 0.6 \end{cases} \qquad [36]$$

In the above, the simple linear relationship between cell voltages of 0.6-0.8 V and the average current density of the cell is employed to reflect the dependence of the interfacial liquid coverage on current density for illustrative purposes. Further, we have neglected the local distribution of interfacial liquid saturation along the flow direction in this first exploration of the interfacial droplet phenomena.

The parameter S_0 is treated as a constant in the following numerical investigation, and its effects on cathode flooding and cell performance are numerically evaluated. While the expressions (Eq. 35 and 36) are highly simplified, their use in this work serves the purpose of demonstrating the new predictive capabilities of the present model.

In summary, the present model for two-phase flow and flooding dynamics in a PEFC consists of four submodels, namely, the catalyst coverage model in the catalyst layer, the two-phase GDL model, the interfacial liquid coverage model at the GDL/GC interface, and the mist flow model for liquid-gas flow in the gas channel.

Results and Discussion

In this section, the two-phase model presented in the preceding section is applied to simulate the two-phase dynamics in a single straight-channel PEFC, with particular focus on the impact of the interfacial liquid coverage model at the GDL/GC interface. The cell is schematically shown in Fig. 1, with its dimensions listed in Table I. Fully humidified hydrogen and air are fed to the anode and cathode inlets, respectively. An inlet stoichiometric ratio of 2 is used on both anode and cathode sides based on a reference current density of 1 A/cm^2; that is, these simulations are for fixed flow rates of anode and cathode gases. The cell operates at a constant temperature of 80°C, and the pressure is 2 atm in both anode and cathode. No contact resistance in the cell is considered in the present numerical study. Other relevant physicochemical and transport parameters are listed in Table II.

Figure 2 compares the polarization curves predicted by the single-phase model where liquid water transport is ignored and the present two-phase model where an interfacial liquid saturation, S_0,
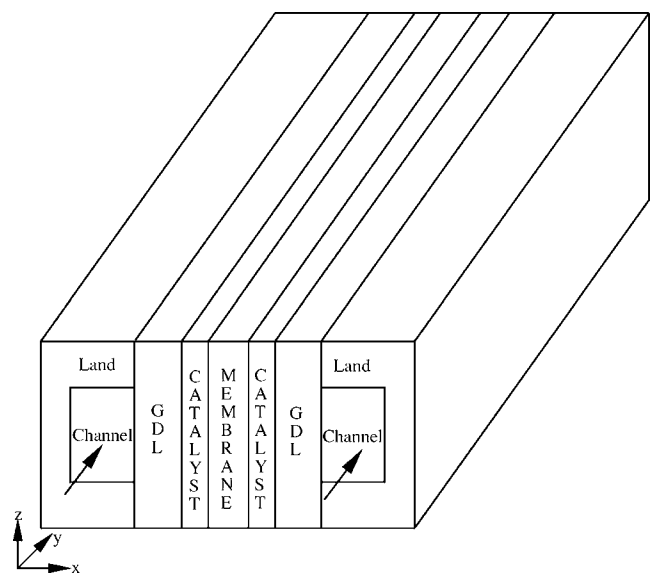
Figure 1. Geometry of a single straight-channel PEMFC.

Table II. Physicochemical parameters.

Anode volumetric exchange current density, aj_0 (A/m^3)	1.0×10^9
Cathode volumetric exchange current density, aj_0 (A/m^3)	1.0×10^4
Reference hydrogen concentration, C_{H_2} (mol/m^3)	40
Reference oxygen concentration, C_{O_2} (mol/m^3)	40
Anode transfer coefficients	$\alpha_a = \alpha_c = 1$
Cathode transfer coefficient	$\alpha_c = 1$
Faraday constant, F (C/mol)	96,487
GDL porosity	0.6
Porosity of catalyst layer	0.12
Volume fraction of ionomer in catalyst layer	0.4
GDL permeability (m^2)	1.0×10^{-12}
Equivalent weight of ionomer (kg/mol)	1.1
Dry membrane density (kg/m^3)	1980
Universal gas constant (J/mol K)	8.314
Electronic conductivity in current collector (S/m)	20,000
Effective electronic conductivity in GDL (S/m)	3000
Operation temperature (°C)	80
Operation pressure (atm)	2
Anode stoichiometry	2
Cathode stoichiometry	2
Liquid water density (kg/m^3)	1000
Liquid water viscosity (N s/m^2)	3.5×10^{-4}
Surface tension (N/m)	6.25×10^{-2}
Contact angle (°)	110
Diffusivity correction factor (τ_d)	1.5
Catalyst coverage coefficient (τ_c)	1.0

of 0.35 is assumed. The two-phase prediction reaches a maximum current density of approximately 1.2 A/cm^2, which is 20% lower than the mass-transport-limited current density of 1.5 A/cm^2 in the single-phase calculation. The difference is attributed entirely to the cathode flooding effect.

If we use the liquid saturation level in the catalyst layer to quantify the degree of PEFC flooding, then there are two possibilities to obtain a high liquid saturation characteristic of GDL/catalyst layer flooding. One is to apply a nonzero interfacial liquid saturation, say 0.35 as in the above simulation, and consequently the liquid saturation is overall high inside the GDL and catalyst layer. The other theoretical possibility is not considering the interfacial liquid coverage but using an unrealistically low GDL permeability so that the liquid saturation gradient across the GDL thickness becomes high. Both scenarios are simulated here and contrasted in Fig. 3 in terms of the liquid saturation distribution in the cathode GDL cross section near the inlet region ($y/y_0 = 0.1$, where y_0 is the cell length). In the case with GDL interfacial coverage, as shown in Fig. 3a (with an average current density of 1.18 A/cm^2 at a cell voltage of 0.60 V), the maximum liquid saturation inside the GDL reaches around 37%, and the liquid saturation variation across the GDL is very small, ranging from 35% at the GDL surface to 37% deep inside. This small spatial gradient is due to the fact that both capillary force and liquid relative permeability are substantially high in the high-saturation regime. Physically, the entire GDL is indeed flooded by a large amount of liquid water. However, the GDL flooding originated from its surface; that is, the flooding is controlled by the interfacial processes occurring on the GDL surface, such as the surface wettability and gas flow conditions in the vicinity. Bulk transport parameters such as GDL thickness and permeability are less influential.

Doubling the GDL thickness would modify the highest liquid saturation from 37 to 39% only. This mechanism for cathode flooding is herein termed as interfacial-transport controlled.

In contrast, in the theoretical case without GDL interfacial coverage but with an exceedingly small permeability (e.g., 10^{-15} m^2), the predicted liquid saturation contour is shown in Fig. 3b (with an average current density of 1.19 A/cm^2 at a cell voltage of 0.65 V). The maximum liquid saturation inside the GDL section is found to be approximately 29%. Note that the practical GDL permeability is on the order of 10^{-12} m^2 so the 3 orders-of-magnitude lower value used in this second case is intended for a hypothetical study only. The striking difference in liquid saturation distribution between Fig. 3a and b is that the high liquid saturation is attained in Fig. 3b by a sharp gradient across the GDL thickness. This implies that the cathode flooding in the latter case is caused by the bulk transport process across the GDL thickness where the GDL thickness and permeability are most critical in influencing the liquid saturation gradient and
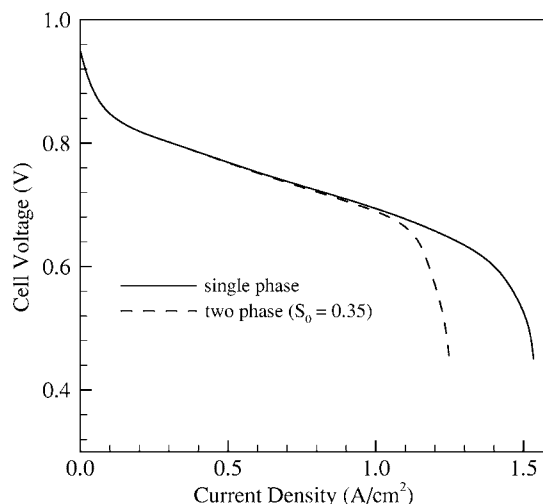
Table I. Cell geometry.

Fuel cell geometry (mm)		
Cell length		100
Gas channel	Depth	1
	Width	1
Layer thickness	Diffusion	0.3
	Catalyst	0.01
	Membrane	0.025
Land width		0.5
Computational cell numbers		~310,000

Figure 2. Polarization curves from single- and two-phase calculations.
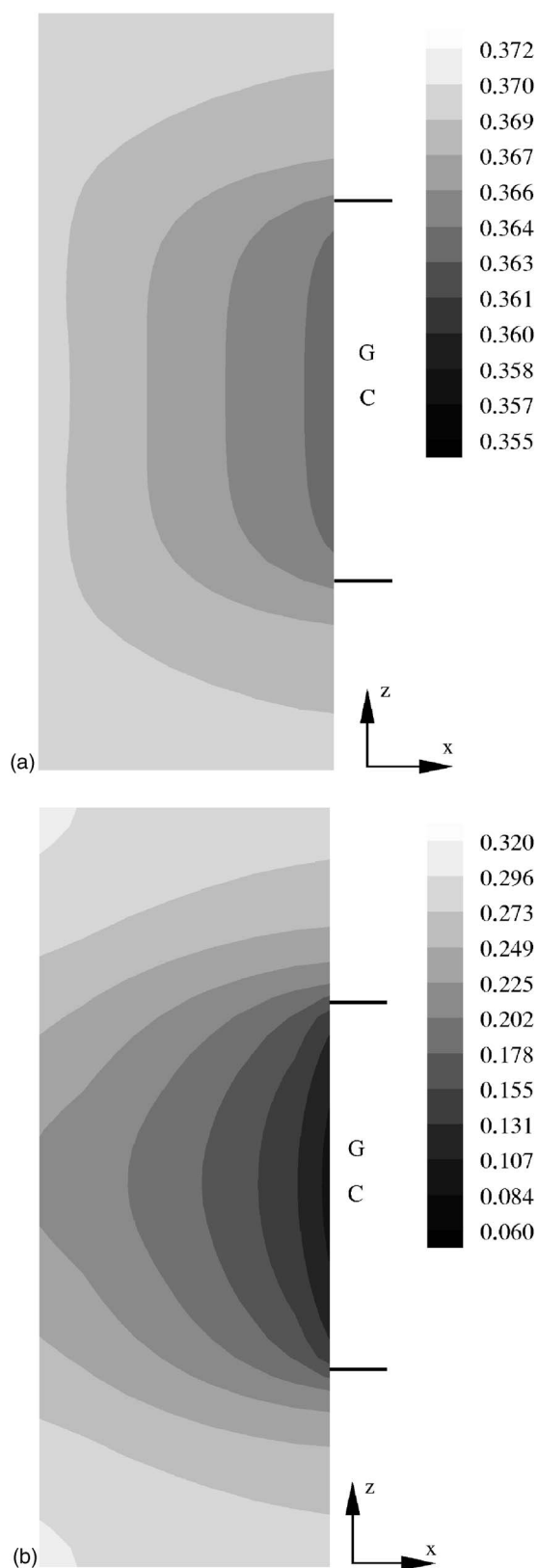
(a)

(b)

Figure 3. Liquid saturation distributions in the cross section perpendicular to the membrane in the cathode GDL near the inlet region ($y/y_0 = 0.1$) at cell voltage of 0.6 V: (a) with interfacial liquid coverage model and (b) without coverage model.

hence its maximum value in the catalyst layer. This mechanism of cathode flooding is termed as bulk-transport-controlled, which is

distinctively different from the interfacial-transport-controlled one. We believe that cathode flooding in reality lies between these two extremes and both mechanisms play a role, with their relative importance depending on GDL materials and cell operating conditions.

The two flooding mechanisms can also be observed in another cross section of the cathode GDL near the outlet region ($y/y_0 = 0.9$), as shown in Fig. 4. Again, in Fig. 4a with GDL interfacial liquid coverage, the liquid saturation is uniformly high inside the entire GDL. In addition, maximal flooding appears in the region under the channel, thus directly blocking oxygen access to the catalyst layer and significantly decreasing cell performance. The liquid saturation distribution in the second case (i.e., without interfacial coverage but with the small permeability) features high nonuniformity, as seen from Fig. 4b. Moreover, the highest liquid saturation or maximal flooding occurs in the land region of the GDL, instead.

Liquid saturation distributions in the plane parallel to the membrane at the catalyst layer/GDL interface are presented in Fig. 5, again for both cases with and without interfacial liquid coverage. While Fig. 5a shows relatively uniform liquid water distribution from the inlet to outlet, Fig. 5b displays substantial variations both along the flow direction (corresponding to the current density distribution) and in the lateral direction from the channel to land regions. The dramatic feature that the GDL will be flooded uniformly once interfacial liquid coverage is applied is more clearly displayed in Fig. 6 where the average liquid saturation at the catalyst layer-GDL interface is plotted along the cathode flow.

Flooding effects on current density distributions in the along-channel direction are shown in Fig. 7 for cell voltages of 0.6 and 0.5 V. In Fig. 7a, the current density profile from the two-phase calculation is significantly lower than that from the single-phase calculation, clearly showing the cathode flooding effect on cell performance. The largest difference between the two curves exists near the inlet region, while the difference diminishes toward the outlet. This trend becomes more apparent at a low cell voltage of 0.5 V as shown in Fig. 7b. The reason for this phenomenon is that the lower current density near the inlet region in the two-phase calculation consumes less oxygen and leaves more oxygen to the outlet region, therefore raising the current density there. At a lower cell voltage and thus higher current density, more oxygen is consumed at the inlet region, rendering less oxygen available downstream. In other words, the current density from the two-phase model, though lower in magnitude, is relatively more uniform than that from the single-phase model.

Lateral current density distributions from both two- and single-phase calculations are compared in Fig. 8 at two locations. In Fig. 8a near the inlet region ($y/y_0 = 0.1$), cathode flooding results in lower current density in the two-phase calculation. The largest difference between the two- and single-phase results occurs in the land region due to the accumulation of more liquid water, as shown in Fig. 3a. An interesting consequence of GDL flooding is that it causes a steeper current density variation in the in-plane direction from the channel to land. The largest difference in the local current density amounts to greater than 1.0 A/cm^2 from the channel to land in the two-phase calculation, while this is only a little over 0.3 A/cm^2 in the single-phase prediction. Near the outlet region ($y/y_0 = 0.9$) shown in Fig. 8b, the difference in the current density profile between the single- and two-phase calculations diminishes for two reasons. First, under the single-phase condition, the oxygen concentration near the outlet region is very low, limiting its diffusion to the area under the land. This results in the steeper current density difference from the channel to land. Second, under the two-phase condition, more oxygen remains near the outlet region because of the lower current density and hence less oxygen consumption at the inlet region. In fact, as shown in Fig. 7, near the outlet region, the difference in the average current density between the single- and two-phase calculations becomes smaller.

In summary, cathode flooding not only lowers cell performance but also results in greater current density nonuniformity in the in-plane direction from channel to land. This is also shown clearly in
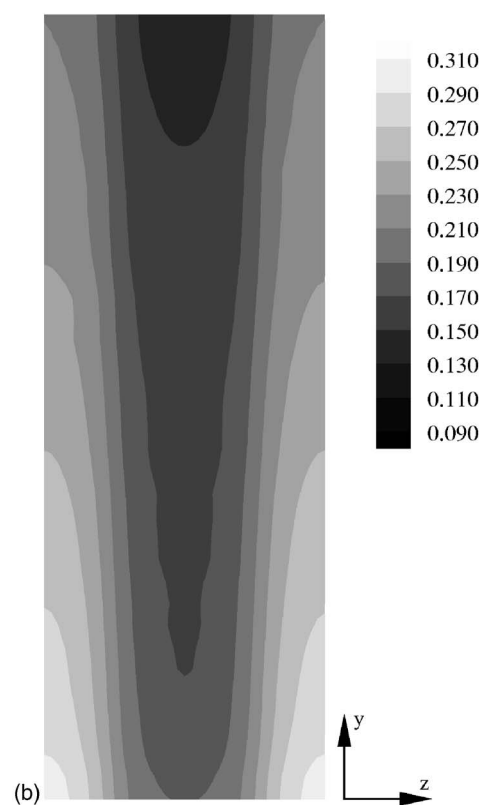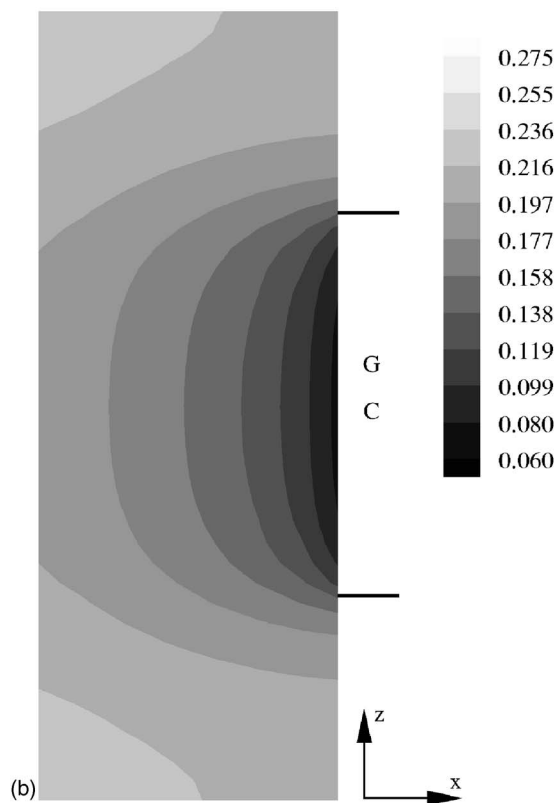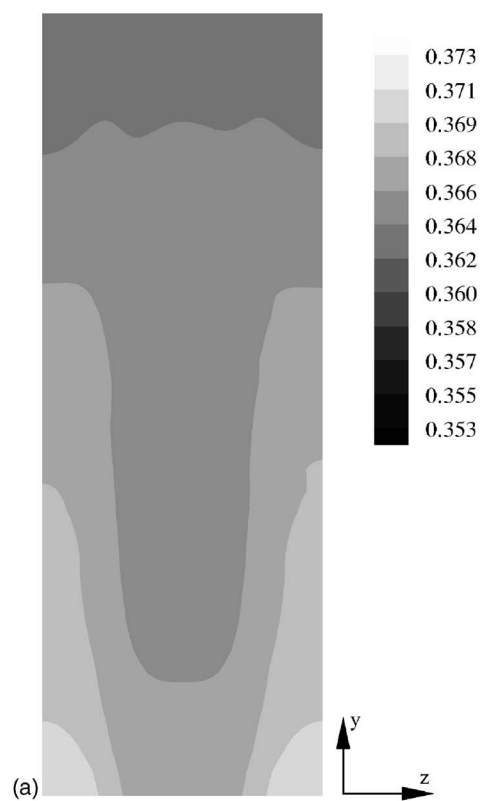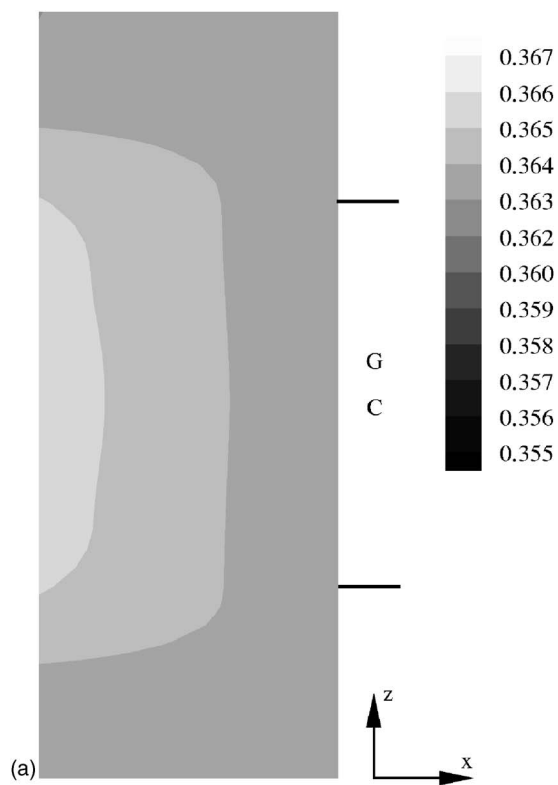
Figure 4. Liquid saturation distributions in the cross section perpendicular to the membrane in the cathode GDL near the outlet region ($y/y_0 = 0.9$) at cell voltage of 0.6 V: (a) with interfacial liquid coverage model and (b) without coverage model.

Figure 5. Liquid saturation distributions in the plane parallel to the membrane in the cathode GDL at cell voltage of 0.6 V: (a) with interfacial liquid coverage model and (b) without coverage model.
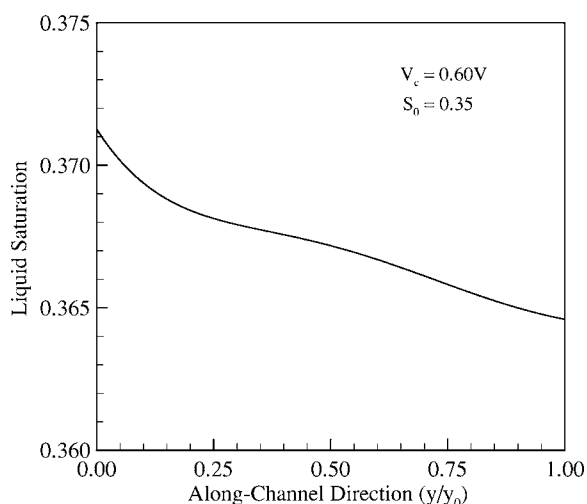
Figure 6. Average liquid saturation profile along the channel direction at the GDL and catalyst layer interface.
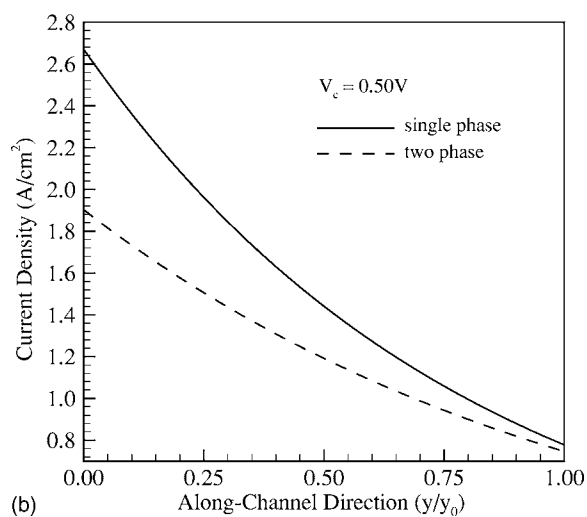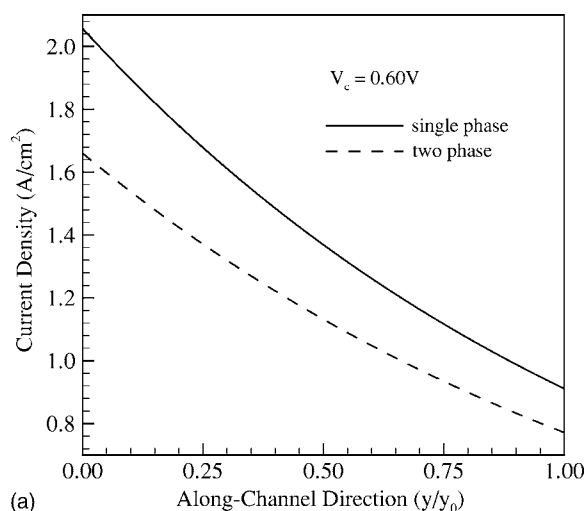

(a)

(b)

Figure 7. Current density profiles along the channel direction from single- and two-phase calculations at: (a) 0.60 and (b) 0.50 V.
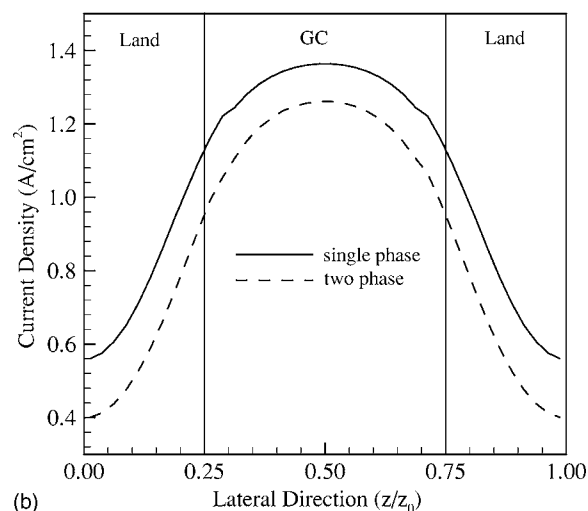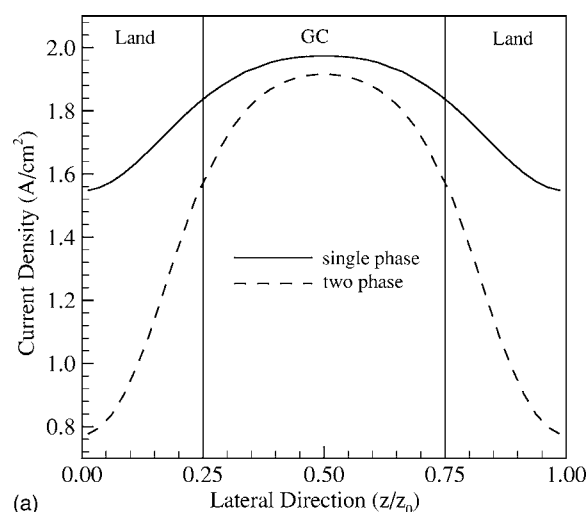

Figure 8. Current density profiles in the lateral direction from single- and two-phase calculations at cell voltage of 0.6 V: (a) near inlet region ($y/y_0 = 0.1$) and (b) near outlet region ($y/y_0 = 0.9$).

Fig. 9, where the contour plots of the current distribution in the middle of the membrane from both two- and single-phase calculations are compared.

With the inclusion of the GDL interfacial liquid coverage, the present model brings about a new capability to investigate the effect of air velocity on cathode flooding. Physically, increasing the air velocity in the gas channel (i.e., the inlet stoichiometry) will decrease the interfacial liquid saturation by more effectively removing liquid droplets from the GDL surface, thereby alleviating the flooding effect on cell performance. This effect can thus be modeled indirectly by decreasing the liquid saturation value, S_0, in Eq. 35 with increasing air stoichiometry. Here we decrease the liquid saturation value (S_0) from 0.35 to 0.18. Figure 10 displays two polarization curves obtained under the two interfacial liquid saturations. It is seen that decreasing the degree of interfacial liquid coverage by means of large air velocity traveling through the gas channel, indeed, significantly benefits the cell performance. With $S_0 = 0.18$, the flooding effect on the mass-transport limiting current density is less than 8% as compared to the single-phase result, while the effect is around 20% with $S_0 = 0.35$ as shown in Fig. 2.

Finally, we employ the mist flow model to describe liquid water transport through the gas channel. This is to assume that liquid is removed from the channel at the same speed as the gas. Under this assumption, the liquid volume fraction in the gas channel is calcu-
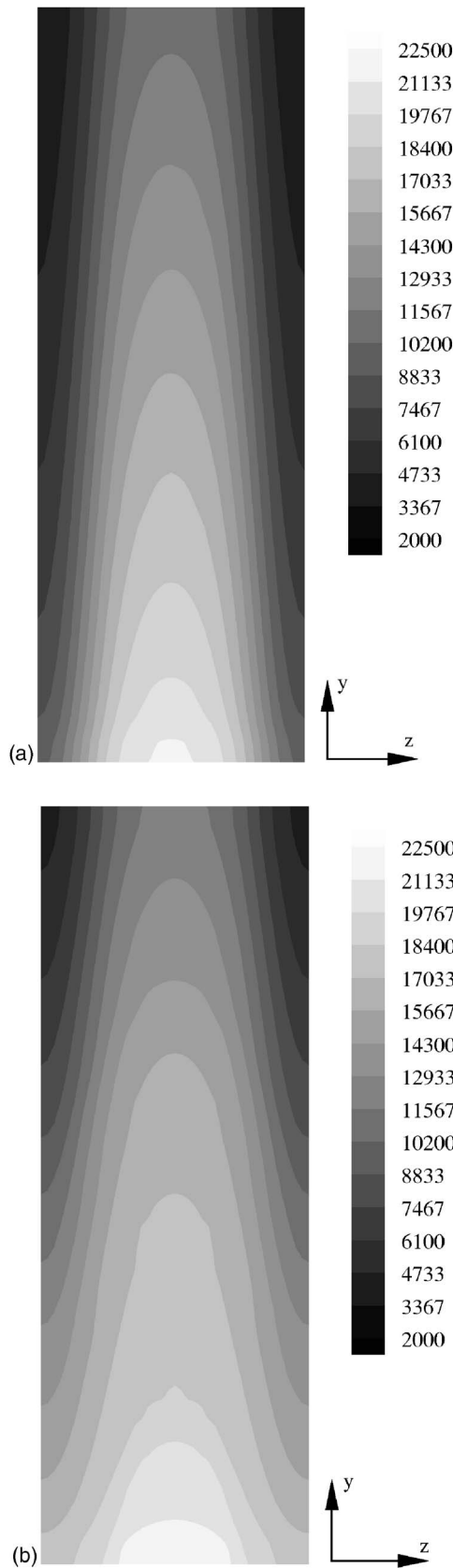
(a)

(b)

Figure 9. Current distributions in the middle of the membrane at cell voltage of 0.6 V from (a) two-phase and (b) single-phase calculations (unit: A/m^2).

lated and shown in Fig. 11. It is seen that the amount of liquid water in the gas channel is gradually increasing from the inlet to outlet, but the liquid volume fraction remains very small, on the order of
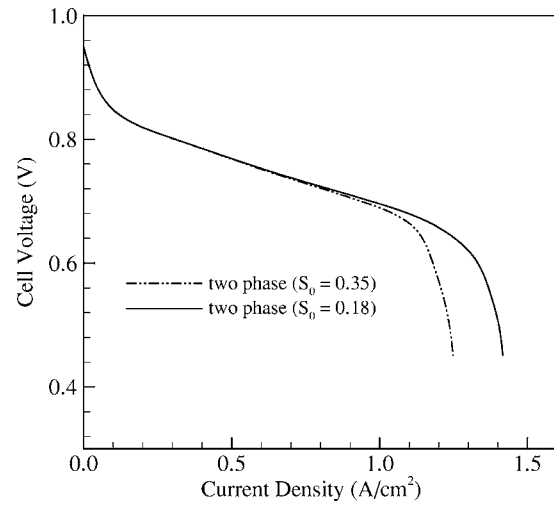

Figure 10. Polarization curves from two-phase calculations using different interfacial liquid saturation values to simulate the air stoichiometry effect.

0.02%, obviously due to the tremendously large liquid removal velocity implied in the mist flow model. Liquid water transport through the gas channel still requires significant modeling effort and particularly the consideration of intricate interactions between liquid water and channel walls under surface tension and wetting conditions characteristic of PEFC bipolar plate materials.

Conclusion

In this paper, a new model for two-phase flow and flooding dynamics in a PEFC has been presented. Particularly, an interfacial
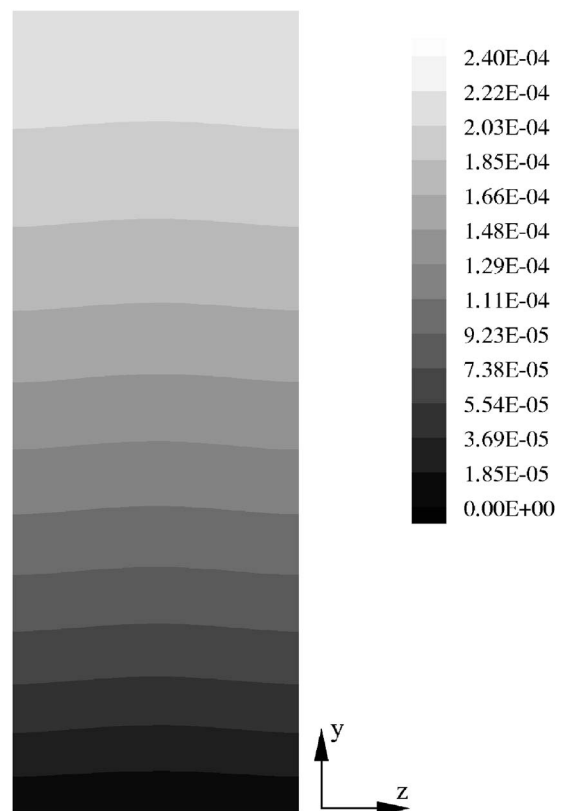

Figure 11. Liquid volume fraction distribution in the middle of cathode gas channel parallel to the membrane at 0.60 V.

liquid coverage model on the GDL surface is integrated for the first time, as prompted by the most recent experimental observations. Addition of this GDL interfacial model lends the present two-phase model new capabilities to predict the electrode flooding effect without resorting to use of unrealistic GDL permeability, ultimately capturing the dramatic effect of air stoichiometry on two-phase dynamics of PEFCs, and potentially differentiating hydrophilic from hydrophobic GDLs in their effects of electrode flooding and cell performance. Furthermore, the present model points to two distinctive mechanisms for electrode flooding: one is controlled by the bulk transport of liquid water across the GDL thickness, and the other dictated by the interfacial processes occurring at the GDL surface.

Acknowledgments

List of Symbols

a	water activity or specific electrochemically active area, m^2/m^3
C	molar concentration, mol/m^3
D	mass diffusivity, m^2/s
e	electron
EW	equivalent weight of dry membrane, kg/mol
F	Faraday constant, 96487 C/mol
$\mathbf{i_e}$	current density vector in the electrolyte, A/m^2
$\mathbf{j}$	transfer current density, A/m^3, or mass flux vector, $mol/(m^2\ s)$
$\mathbf{J}$	Leverett function
k_r	relative permeability
K	permeability, m^2
Mw	molecular weight, kg/mol
M_i	Species symbol
n	number of electrons in electrochemical reaction
n_d	electro-osmotic drag coefficient
p	pressure, Pa
R	universal gas constant, 8.314 $J/(mol\ K)$
s	stoichiometry coefficient in electrochemical reaction liquid saturation
S	source term in transport equation
S_0	liquid saturation function
T	temperature, K
u	fluid velocity and superficial velocity in porous medium, m/s
U_{oc}	open-circuit potential, V
V	volume, m^3
V_c	cell voltage, V

Greek

α	transfer coefficient
ε	porosity
λ	water content in membrane relative mobility
Φ	phase potential, V
γ	advection correction factor
η	overpotential, V
μ	viscosity, $kg/(m\ s)$
ν	kinematic viscosity, m^2/s
θ	contact angle
ρ	density, kg/m^3
κ	proton conductivity, S/m
σ	electronic conductivity, S/m surface tension, N/m
τ	viscous force tensor

Superscripts

eff	effective value
m	membrane
τ_c	catalyst coverage coefficient
τ_d	diffusivity coefficient
ref	reference value
sat	saturation value

Subscripts

a	anode
c	cathode or capillary
e	electrolyte
g	gaseous phase
i	species index
int	interface
k	phase index, either liquid or gas
l	liquid phase
m	mixture or membrane
oc	open circuit
p	pore
s	electron
w	water

References

1. V. Gurau, H. Liu, and S. Kakac, *AIChE J.*, **44**, 2410 (1998).
2. J. S. Yi and T. V. Nguyen, *J. Electrochem. Soc.*, **146**, 38 (1999).
3. S. Um, C. Y. Wang, and K. S. Chen, *J. Electrochem. Soc.*, **147**, 4485 (2000).
4. S. Dutta, S. Shimpalee, and J. W. Van Zee, *J. Appl. Electrochem.*, **30**, 135 (2000).
5. S. Um and C. Y. Wang, *J. Power Sources*, **125**, 40 (2004).
6. S. Shimpalee and S. Dutta, *Numer. Heat Transfer, Part A*, **38**, 111 (2000).
7. T. Berning, D. M. Lu, and N. Djilali, *J. Power Sources*, **106**, 284 (2002).
8. S. Mazumder and J. V. Cole, *J. Electrochem. Soc.*, **150**, A1503 (2003).
9. H. Meng and C. Y. Wang, *J. Electrochem. Soc.*, **151**, A358 (2004).
10. H. Ju, H. Meng, and C. Y. Wang, *Int. J. Heat Mass Transfer*, **48**, 1303 (2005).
11. H. Meng and C. Y. Wang, *Chem. Eng. Sci.*, **59**, 3331 (2004).
12. Z. H. Wang, C. Y. Wang, and K. S. Chen, *J. Power Sources*, **94**, 40 (2001).
13. C. Y. Wang and P. Cheng, *Int. J. Heat Mass Transfer*, **39**, 3607 (1996).
14. C. Y. Wang and P. Cheng, *Adv. Heat Transfer*, **30**, 93 (1997).
15. L. You and H. Liu, *Int. J. Heat Mass Transfer*, **45**, 2277 (2002).
16. S. Mazumder and J. V. Cole, *J. Electrochem. Soc.*, **150**, A1510 (2003).
17. U. Pasaogullari and C. Y. Wang, *J. Electrochem. Soc.*, **152**, A380 (2005).
18. T. Berning and N. Djilali, *J. Electrochem. Soc.*, **150**, A1598 (2003).
19. J. Bear, *Dynamics of Fluids in Porous Media*, Elsevier, New York (1972).
20. W. He, J. S. Yi, and T. V. Nguyen, *AIChE J.*, **46**, 2053 (2000).
21. D. Natarajan and T. V. Nguyen, *J. Electrochem. Soc.*, **148**, A1324 (2001).
22. K. Tüber, D. Pócza, and C. Hebling, *J. Power Sources*, **124**, 403 (2003).
23. X. G. Yang, F. Y. Zhang, A. L. Lubawy, and C. Y. Wang, *Electrochem. Solid-State Lett.*, **7**, A408 (2004).
24. C. Y. Wang, *Chem. Rev. (Washington, D.C.)*, **104**, 4727 (2004).
25. F. Y. Zhang, X. G. Yang, and C. Y. Wang, *J. Electrochem. Soc.*, To be submitted
26. U. Pasaogullari and C. Y. Wang, *J. Electrochem. Soc.*, **151**, A399 (2004).
27. C. Berger, *Handbook of Fuel Cell Technology*, Prentice-Hall, Englewood Cliffs, NJ (1968).
28. T. A. Zawodzinski, J. Davey, J. Valerio, and S. Gottesfeld, *Electrochim. Acta*, **40**, 297 (1995).
29. F. N. Büchi and G. C. Scherer, *J. Electrochem. Soc.*, **148**, A183 (2001).
30. T. E. Springer, T. A. Zawodzinski, and S. Gottesfeld, *J. Electrochem. Soc.*, **138**, 2334 (1991).
31. S. Motupally, A. J. Becker, and J. W. Weidner, *J. Electrochem. Soc.*, **147**, 3171 (2000).
32. J. H. Nam and M. Kaviany, *Int. J. Heat Mass Transfer*, **46**, 4595 (2003).